Molecular beam epitaxial growth of multilayer 2D-boron nitride on Ni substrates from borazine and plasma-activated nitrogen

Jawad Hadid, Ivy Colambo, Jose Avila, Aexandre Plaud, Christophe Boyaval, D. Deresmes, Nicolas Nuns, Pavel Dudin, Annick Loiseau, Julien Barjon, et al.

Molecular beam epitaxial growth of multilayer 2D-boron nitride on Ni substrates from borazine and plasma activated nitrogen

Jawad Hadid[1], Ivy Colambo[2], Jose Avila[3], Alexandre Plaud[4,5], Christophe Boyaval[1], Dominique Deresmes[1], Nicolas Nuns[6], Pavel Dudin[3], Annick Loiseau[5], Julien Barjon[4], Xavier Wallart[1], Dominique Vignaud[1*]

[1]*Univ. Lille, CNRS, Centrale Lille, JUNIA ISEN, Univ. Polytechnique Hauts de France, UMR 8520-IEMN F-59000 Lille France*

[2]*Inst. Math. Sci. Phys., Univ. of the Philippines Los Banos, Laguna 4031 Philippines*

[3]*Synchrotron SOLEIL & Université Paris-Saclay, F-91192 Gif sur Yvette France*

[4]*Université Paris-Saclay,UVSQ, CNRS, Groupe d'Etude de la Matière Condensée, 45 avenue des Etats-Unis,78035 Versailles Cedex, France*

[5]*Laboratoire d'Etude des Microstructures (LEM), CNRS–ONERA, Université Paris Saclay, 29 Avenue de la Division Leclerc, 92320 Chatillon, France*

[6]*Univ. Lille, CNRS, Centrale Lille, ENSCL, Univ. d'Artois, IMEC-Institut Michel-Eugène Chevreul 59000 Lille France*

**corresponding author: dominique.vignaud@univ-lille.fr*

Abstract:

2D boron nitride (2D-BN) was synthesized by gas-source molecular beam epitaxy on polycrystalline and monocrystalline Ni substrates using gaseous borazine and active nitrogen generated by a remote plasma source. The excess of nitrogen atoms allows to overcome the thickness self-limitation active on Ni when using borazine alone. The nucleation density and the shape of the 2D-BN domains are clearly related to the Ni substrate preparation and to the growth parameters. Based on spatially-resolved photoemission spectroscopy and on the detection of the π plasmon peak, we discuss the origin of the N1s and B1s components and their relationship with an electronic coupling at the interface. After optimization of the growth parameters, a full 2D-BN coverage is obtained, although the material thickness is not evenly distributed. The 2D-BN presents a granular structure on (111) oriented Ni grains, showing a rather poor cristallographic quality. On the contrary, high quality 2D-BN is found on (101) and (001) Ni grains, where triangular islands are observed whose lateral size is limited to ~20 µm.

1. Introduction:

Among the two-dimensional materials, graphene occupies a remarkable position with its exceptional electronic properties, including an electron mobility that can exceed 10^6 cm²/V.s [1]. However, exploiting these properties in devices remains a challenge. Indeed, due to its monolayer thickness, the properties of graphene depend strongly on the substrate on which it is deposited. Many studies have recently shown that hexagonal boron nitride (hBN) is a suitable material for preserving the electronic properties of graphene. With a lattice mismatch of 1.6% [2, 3], van der Waals inter-planar bonds [4], a wide band gap of ~6.25 eV [5], hBN has proven to be an ideal layer for support and encapsulation of graphene [6]. Hence, hBN would be a way to passivate graphene and take advantage of its exceptional electronic properties.

Despite advances in hBN growth techniques, current research is facing two major challenges: the growth of large scale hBN with a thickness control efficient down to the monolayer and the fabrication of graphene/hBN heterostructures. Compared to graphene where the growth of a monolayer can occur by a purely surface mechanism due to the low solubility of carbon in the substrate [6], the growth processes of 2D-BN are more complex. A balance of two elements, B and N, is required to form hBN. The stoichiometry is expected to be ensured by the use of molecules such as borazine ($B_3N_3H_6$) for which the B/N ratio is 1, as is the case for hBN. This gaseous precursor was used on many metallic substrates, for example Ni, Rh, Pt [7-9] in ultra-high-vacuum (UHV) environment. Because the fragmentation of the borazine molecules is catalysed by the metallic nature of the substrate, the growth is often limited to one hBN layer [7]. Other studies used different precursors for B and N, which made it possible to overcome this thickness limitation. For example, elemental boron was combined with N_2 activated in a plasma cell [10-12]. Alternative sources were used, such as B_2O_3 powder [13] or a combination of NH_3 and B_2H_6 gases [14]. Only one study recently reported the growth of hBN from a combination of borazine and N_2 activated in a plasma cell [15]. Multilayers could be obtained on epitaxial graphene on SiC, although the high pressures used (~10^{-3} Torr) could result in a rather poor control of the hBN thickness for few monolayer thick films.

In this article, we study the effect of an excess of nitrogen in the incoming flux on the growth of BN on Ni under UHV conditions. The precursors were borazine associated to active nitrogen generated by a plasma source, a configuration rather similar to the one used in Ref. 15 although at lower working pressures in our case. The growth parameters (temperature, duration, precursor flux ratio) have been optimized and the effect of the Ni grain orientation has been highlighted. The influence of the Ni orientation on the growth and the structure of hBN domains was already explored by different groups, with a particular emphasis on the hBN growth rate [16-18], by low-pressure chemical vapor deposition. Using ammonia-borane at 10 Torr, the growth was found faster on (001) oriented surfaces while no hBN could be detected on (111) grains [16]. This conclusion was partially confirmed in Ref. 17, who observed that the thickest hBN was obtained on (101) or (001) orientations, although they also found thinner BN on (111) surfaces, using a borazine/hydrogen mixture at ~6 mTorr. This result was attributed to the surface energy of Ni grains decreasing in the same order (101), (001) and (111) [19]. On the other hand, the highest growth rate was observed on (101), followed by (111) and then (001) surfaces, also using poly-crystalline Ni substrates but with ammonia and

diborane precursors at ~0.7 Torr [18]. This effect was attributed to the orientation-dependent rates of segregation and diffusion of boron and nitrogen. Clearly, the importance of the crystalline orientation of Ni is not yet well understood and may depend on the growth techniques, e.g. on the working pressure or the precursors used. The criteria used to assess the quality of a material must also be selected with care. The comparison of the main hBN E_{2g} Raman peak intensity used in the previously mentioned articles may not be the most suitable way to compare the quality of the synthetized hBN, since it also depends on its thickness [20]. Furthermore, in the case of hBN on Ni, a strong hybridization occurs at the interface between the Ni 3d and BN π states, making the hBN monolayer to behave as a metal [21, 22]. The lack of detection of the hBN main Raman peak may be due to this strong bonding [23], thus leading to an erroneous conclusion about the absence/presence of hBN. It must be finally mentioned that another 2-dimensional BN structure than hBN is possible, involving a rhombohedral stacking (rBN) [24]. Both are based on the same elementary brick, the hexagonal BN plane, and only differ by the stacking of the BN layers on top of each other. The stacking is ABC for rBN and AA' for hBN. They present very similar characteristics, e.g. an identical B/N composition ratio, a main Raman E_{2g} peak at ~1370 cm^{-1}. Both have a large band gap around ~6 eV [25] and are not easily identifiable. So, we are using the generic term 2D-BN for the 2D material BN grown in this study, since its exact stacking is not yet determined.

2. Experimental methods:

All growth experiments were carried out in a commercial Riber molecular beam epitaxy (MBE) chamber under UHV conditions. The growth temperature was set between 700 and 980°C. All details about the borazine set-up can be found in a previous article [23]. Most important for this study, the borazine flux is controlled by a regulating pressure system located between the borazine cylinder and a calibrated 0.25 mm diameter hole. For a regulation set at $P_{borazine}$ = 0.1 or 1 Torr, the pressure in the growth chamber is $3.5x10^{-8}$ or $4.5x10^{-7}$ Torr respectively. The activated nitrogen was generated by a Riber radio-frequency valve plasma cell (VRF-N-600), working in the 450-540 W power range. When combining borazine with activated nitrogen, the measured pressure increases up to ~10^{-5} Torr. The high purity nitrogen (99.9999%) flux is regulated by a 10 sccm mass flow controller, with a N_2 flow set between 0.5 and 1.5 sccm. The light intensity emitted by the nitrogen plasma V_{N2} is measured (in volts) by an optical sensor sensitive in the 750-850 nm wavelength range, corresponding mainly to atomic nitrogen [26]. Assuming that the output signal from this sensor is a direct measure of the active nitrogen flux involved in the growth [27], the ratio B:N of the molecular fluxes arriving at the surface of the sample is therefore approximated by $R_{B/N2}$, the ratio between the regulated pressure of borazine and the V_{N2} signal. This ratio is thus expressed in Torr/V.

Two different kind of 1x1 cm^2 nickel substrates were used, polycrystalline foils and (111) monocrystals. The 25 µm thick Ni foils were purchased from Alfa-Aesar and cut into pieces. The (111) substrates were supplied by Alineason (thickness 1 mm). A (001) grain of ~2x3 mm^2 surface was detected by electron backscattered diffraction (EBSD) on one monocrystalline (111) substrate. We took advantage of this occurrence to study 2D-BN growth on this orientation. All substrates were ultrasonically cleaned at room temperature for 20 minutes in acetone, then in isopropanol and finally deoxidized at ~50°C in acetic acid for about 15 minutes. Before growth, they were systematically annealed at 1000°C in the MBE chamber for

at least 1 hour. This annealing step aims to eliminate most of the carbonaceous species adsorbed on the Ni substrates [28] and to remove the residual oxygen [29]. In order to increase the grain size [30], a preliminary annealing at 1050°C in a chemical vapor deposition reactor under 10 sccm of hydrogen and a pressure of 10 Torr was also tested. This pre-annealing was followed by the standard 1000°C treatment under UHV.

Everhart-Thornley and Inlens detectors were mainly used in a Zeiss Supra 55 scanning electron microscope (SEM) at an energy of 1 keV. The former is more sensitive to secondary electrons than to backscattered ones. Its image contains information related to the topography of the substrate. The Inlens detector mainly measures electrons backscattered along the beam direction and produces images with high spatial resolution. In the case of hBN, the Inlens intensity depends on the thickness of the deposited material [31]. This electron microscope is also equipped with an Oxford Nordlys detector for performing EBSD analysis to identify the orientations of the Ni grains. A Jeol 7001E SEM was used for cathodoluminescence experiments at low-temperature (5 K) with 2-5 kV electron beam. Spectra were corrected for the spectral sensitivity of the set-up [5, 32]. Raman measurements were made using a Horiba Scientific LabRAM HR confocal Raman spectrometer with a 473 nm laser spot (power ~10 mW) focused to a size smaller than 1 µm by a 100X objective. All spectra discussed in this work were corrected by subtraction of the Ni substrate contribution. They were measured on specific 2D-BN domains, as precisely located by SEM. Conductive atomic force microscopy (c-AFM) images were recorded in contact mode, with a Bruker Icon microscope under ambient conditions. Currents down to the pA range could be detected thanks to a current preamplifier with a variable gain from 10^7 to 10^{11} V/A. Time of flight secondary ion mass spectroscopy (ToF-SIMS) measurements were realized with a TOF SIMS.5 system (Iontof), in burst mode, using 25 keV Bi^+ as primary ion source. The typical spatial resolution is 200 nm. The BN content was studied by measuring the $^{10}BN^-$ signal [33].

Conventional X-ray photoemission spectroscopy (XPS) measurements were realized using a Physical Electronics 5600 spectrometer fitted in an UHV chamber (base pressure ~$1 \cdot 10^{-10}$ Torr). A monochromatized Al anode X-ray source (1487 eV) was used with a typical probe size of ~400 µm diameter. The detection angle was varied between 25° and 75° with respect to the sample surface plane. The B/N composition ratio was determined from the I_{B1s}/I_{N1s} integrated intensity ratio, corrected for the instrument relative sensitivity as calibrated after a measurement on exfoliated hBN. The spectra shown here were all obtained with an angle of 45°. Spatially resolved photoemission was measured at the Antares beamline of the Soleil synchrotron with a photon energy of 700 eV, a photon probe size of ~1.0-1.5 µm diameter and a photoelectron detection direction normal to the sample surface. The samples were annealed at 700°C under UHV conditions before measurements to eliminate any possible contamination resulting from the air transfer. To optimize the beamtime use, only N1s maps were recorded and the presence of π plasmons was only evaluated for the N1s spectrum (nitrogen having a higher sensitivity factor than boron). Angle-resolved photoemission spectroscopy with sub-micron spatial resolution (nanoARPES) was also measured at 100 eV photon energy (see details of the experiments in Ref. 34).

3. Results:

3.1 2D-BN growth optimization:

The typical XPS spectra of hBN exhibit a single B1s peak between 190 and 191 eV and a single N1s one in the range 397.6-398.7 eV [35-37]. A signal originating from the π plasmons should be detected at ~9 eV from the B1s and N1s main peaks to confirm the 2D nature of the material [38, 39]. The B1s and N1s XPS typical spectra of a sample grown using borazine and activated nitrogen are shown in Fig. 1. One component is generally observed for nitrogen (Fig. 1a), while two well-resolved peaks are present for boron (Fig. 1b). The detection of π plasmons at ~9 eV of the main B1s and N1s peaks confirms the 2D character of the synthetized 2D-BN. The origin of the B1s peak at 188.2 eV (Fig. 1b) is not well understood. It could correspond to B-Ni [40, 41] or B-B bonds [40, 42, 43]. As already discussed [23], this peak, not related to BN, is probably associated with interface states and its discussion is beyond the scope of this article. The best fits of the 2D-BN-related B1s and N1s spectra are also shown in Fig.1, using an iterative Shirley baseline. They involve two symmetric components each, with a strongly dominant one at higher binding energy (shown in blue) and a weak one at lower binding energy (in green). This symmetrical shape is consistent with the detection of π plasmons since it implies the presence of 2D-BN not coupled to the substrate [23]. Noticeably, the binding energy difference between the N1s and B1s peaks is identical for the two pairs of high- and low-intensity components (E_{N1s}-E_{B1s} = 207.6 ± 0.1 eV), a typical value for hBN [21]. The B/N composition ratio calculated from the high-intensity components is 1.00 ± 0.05 and corresponds to the expected stoichiometry of 2D-BN. Taken together, these observations show that the high-intensity B1s and N1s components correspond to the planar interactions between B and N atoms in the 2D-BN not interacting with the substrate. The low-intensity peaks are shifted by 0.9 ± 0.1 eV towards lower binding energy from the high-intensity components. Their energy positions are identical to those obtained for monolayer BN with a strong coupling with Ni, grown using borazine only [23]. This similarity suggests that they correspond to the interface BN subjected to strong interactions with the Ni substrate. Indeed, this is confirmed by the B/N composition ratio for the low intensity components which is 1.0 ± 0.2. Larger composition fluctuations were observed for a few samples, that could result from the low accuracy of the fit for these low intensity components (see Fig. 1).

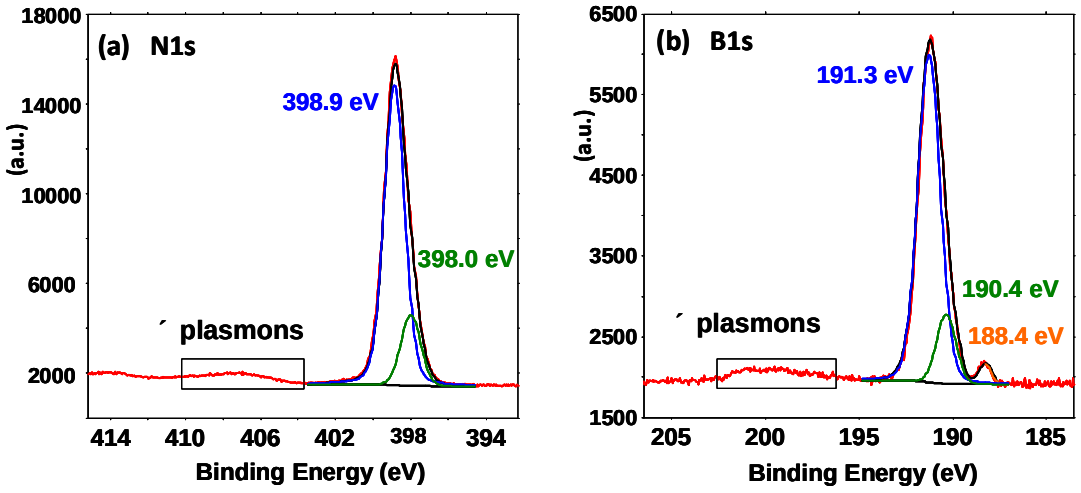

Figure 1: XPS core level spectra for N1s (a) and B1s (b) after 2D-BN growth for 1 hour at 910°C. The π plasmon peaks are shown in the black rectangles. The best fits, using two symmetrical components for both cases, are shown, as well as the Shirley baseline.

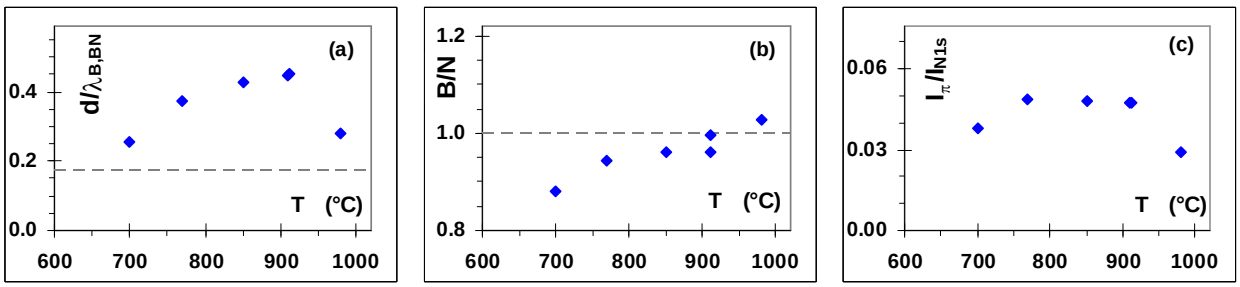

Figure 2: 2D-BN growth optimization, thickness $d/\lambda_{B,BN}$ (a), B/N composition ratio (b) and π plasmon intensity normalized to the total nitrogen peak intensity (c), as a function of the growth temperature. All growth experiments lasted 60 minutes. The dashed lines are just guides, representing the $d/\lambda_{B,BN}$ saturation value obtained when using borazine as the only precursor [23] (a) and the stoichiometric value of the composition ratio (b).

With a constant precursor flux ($P_{borazine}$=1 Torr and V_{N2} = 1.45 V) and growth time (60 min), the amount of deposited 2D-BN on Ni foils, the B/N composition ratio as well as the intensity of the π plasmons normalized to the nitrogen peak intensity were explored as a function of the growth temperature (Fig. 2). The 2D-BN thickness was evaluated using the I_{B1s}/I_{Ni2p} and I_{N1s}/I_{Ni2p} XPS integrated intensity ratio from which the $d/\lambda_{B,BN}$ ratio was calculated (Fig. 2a), where d is the 2D-BN thickness and $\lambda_{B,BN}$ is the inelastic mean free path of photoelectrons emitted from B and passing through 2D-BN. Note that these calculations were based on the total area of the BN-related boron and nitrogen peaks. We used a model based on a uniform 2D-BN film on Ni [23]. Such a simple model may only give rough estimates of the total thickness when the real layer is not homogeneously distributed, as is the case here, but it is the only realistic modeling without introducing multiple unknown fitting parameters. The low intensity components are typically representing ~10% of the total area of the B1s and N1s peaks, so analysis based on the total B1s and N1s area or only on the high intensity components lead to nearly similar estimates. Within these isochronous experiments, the optimum growing temperature range lies between 770°C and 910°C. In this range, the deposited 2D-BN is the thickest (Fig. 2a), has a B/N ratio close to 1 (Fig. 2b) and the ratio of the intensity of the π plasmons to the total N1s intensity is maximum (Fig. 2c). Considering a value of 3.3 nm for $\lambda_{B,BN}$ for conventional XPS experiments [44], the estimated $d/\lambda_{B,BN}$ ratio corresponds to a maximum 2D-BN thickness of 4-5 monolayers (ML) for a 60 min growth. This value clearly exceeds the value that was obtained after growth using borazine alone, which saturates in the 1-2 ML range (see dashed line in Fig 2a) because of the self-limited growth induced by the catalytic effect of the Ni substrate [23]. The excess of nitrogen induced by the N_2 plasma makes it possible to overcome this thickness saturation. Possible mechanisms responsible for this effect may be related either to growth under a N-rich environment or more probably from a significant contribution of the activated nitrogen to the fragmentation of the borazine. In the case of growth at 980°C, the estimated 2D-BN thickness is reduced compared to that at 910°C, the film tends to become B-rich and the relative plasmon intensity decreases. These observations suggest a degradation of the 2D-BN characteristics and may be explained by a lower sticking at least for nitrogen atoms at high temperatures. At the lowest studied temperature of 700°C, the precursors are expected to adsorb at least as efficiently than at higher temperatures, which is inconsistent with the reduction of the estimated thickness shown in Fig. 2a. We suggest that this discrepancy could be explained by an

increased roughness of the 2D-BN film, which would lead to an underestimation of the thickness because of the homogeneous film model used here. An alternative explanation of this lower BN thickness could involve a reduced borazine thermal fragmentation at 700°C compared to 900°C.

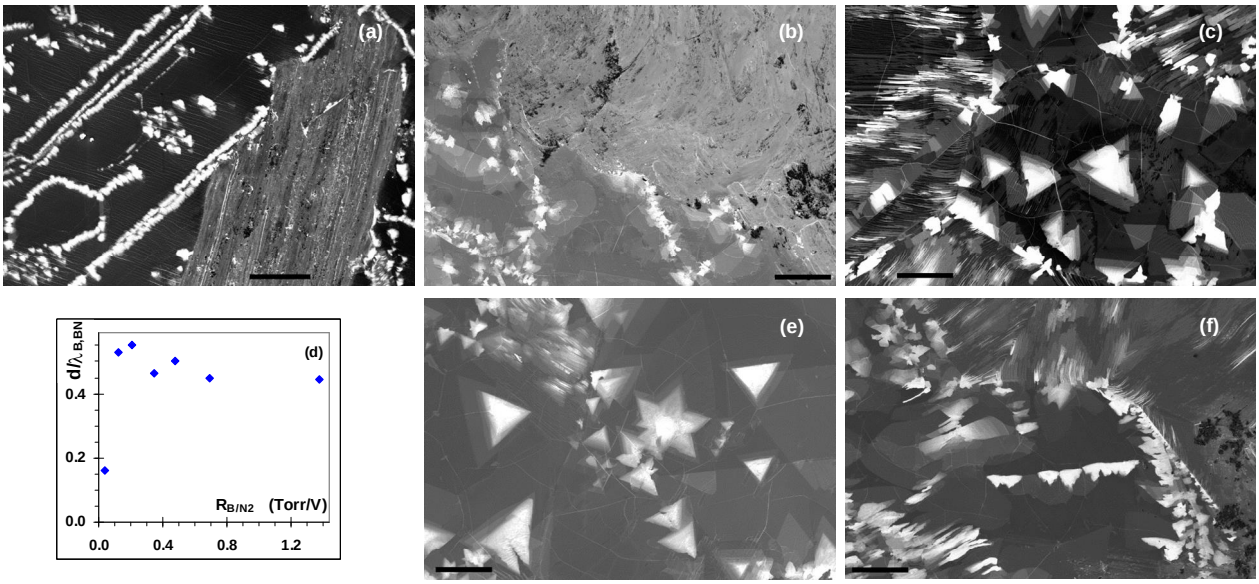

Figure 3: SEM InLens images for 60 min 2D-BN growth with $R_{B/N2}$=0.7 Torr/V, at 770°C (a), 850°C (b) or 910°C (c). 60 min 2D-BN growth at 910 °C, thickness $d/\lambda_{B,BN}$ as a function of the molecular flux ratio $R_{B/N2}$ (d) and SEM InLens images at $R_{B/N2}$=0.2 Torr/V (e) or 1.4 Torr/V (f). All scale bars are 10µm.

SEM Inlens observations of samples grown within the previously determined optimum temperature range are shown in Fig. 3a-c. They were combined with Raman measurements focused on the 2D-BN domains for which the Inlens signal is the most intense, which appear as white triangles in Fig. 3a-c. They correspond to the thickest domains [31]. The minimum full width at half maximum (FWHM) of the 2D-BN Raman E_{2g} peak obtained respectively at 770, 850 and 910°C are 16-19, 15-21 and 10-11 cm^{-1} (see corresponding spectra in the supplementary material Fig. S1). So, the best 2D-BN quality is obtained at 910°C, for which the Raman peak has the smallest width, the composition ratio B/N is 1.0 and the 2D-BN islands show the most regular and largest geometric shapes (see Fig. 3c). The fact that this temperature is optimal is probably due to the higher mobility of ad-atoms at this high temperature, while remaining lower than those for which the sublimation mechanisms become significant (980°C). The characteristic 2D-BN E_{2g} Raman peak was not detected on the samples prepared at 700°C and 980°C having the lowest intensities of π plasmons. The detection of the Raman peak for 2D-BN seems to correlate well with the intensity of the π plasmons (see Fig. 2c). The Raman signal associated to 2D-BN was not detected on the dark domains of the SEM images: this could result from the low BN thickness in these areas [20] and/or from the strong electronic interactions with the Ni substrate for monolayer 2D-BN [23].

The influence of the B:N molecular flux ratio, assumed proportional to the ratio $R_{B/N2}$ previously described, was studied for 2D-BN growth experiments carried out at 910°C within the $R_{B/N2}$ range 0.04-1.4 Torr/V. The E_{2g} Raman peak width, the $d/\lambda_{B,BN}$ factor (see Fig. 3d), the N1s plasmon peak intensity, the shape and size of the 2D-BN domains (Fig. 3e-f) were combined to find that the optimum range is between 0.1 and 0.2 Torr/V. The lowest value of the B:N molecular flux ratio ($R_{B/N2}$ =0.04 Torr/V) leads to a non-stoichiometric, thinner BN film with a very weak N1s plasmon peak. Samples grown using B-richest conditions result in lower quality material as shown by their irregular geometric shape and reduced domain size (compare Fig. 3f to Fig. 3e). Using these optimized growth conditions, we have studied the 2D-BN structure as a function of growth duration. The SEM images of samples grown for 4 and 8 h respectively are shown in Figs. 4a and 4b. It appears that the maximum lateral dimensions of the 2D-BN domains do not grow significantly after 4 h, saturating at a typical value of ~20 µm (Fig. 4c). The thickness of the triangular domains might be estimated by counting the number of stacked triangles in such images (see supplementary material Fig. S7). A maximum thickness is found in the range 10-15 ML (Fig. 4c), assuming that each change of contrast observed in the SEM image correspond to a monolayer step.

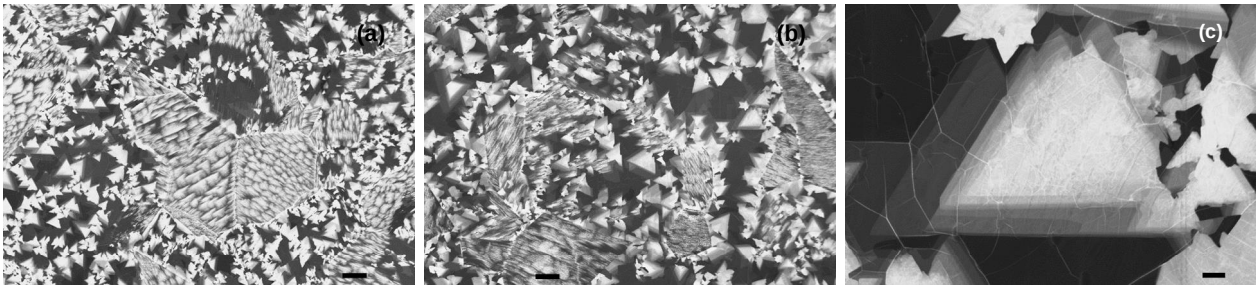

Figure 4: SEM InLens images for 2D-BN growth at 910°C, with $R_{B/N2}$=0.2 Torr/V, for 4 h (a) or 8 h (b). High magnification SEM InLens image after 4h growth highlighting the typical 2D-BN domain size of ~20µm (c). Scale bars are 10 µm (a, b) and 2 µm (c).

The properties of the triangular 2D-BN domains were more extensively characterized. A typical Raman spectrum is shown in Fig. 5a. The peak maximum is found in the 1368-1371 cm^{-1} range, with FWHM down to 10-11 cm^{-1} (see also the Raman mapping analysis which is presented in the supplementary material Fig. S2). Several 2D-BN islands were also studied by cathodoluminescence at 5 K, a typical spectrum being presented in Fig. 5b. No luminescence related to deep defects could be detected in the range from 1.4 up to 5 eV (250-890 nm, see supplementary material part 2), reflecting the low incorporation of impurities in these domains [45]. Only two main contributions are detected: an emission at 5.77 eV is associated to the indirect excitons iX [46] while peaks at 5.37 and 5.51 eV seem related to excitons bound to structural defects [47]. A low intensity peak is also detected at 6.045 eV, that corresponds to the recombination of non-thermalized dX direct excitons in hBN [5]. Furthermore, the luminescence peak corresponding to surface excitons at 5.9 eV in hBN [48] is not detected. If the observation of direct exciton luminescence suggests the high quality of our 2D-BN materials, complementary studies are required to understand the different thickness behavior observed in these spectra compared to previous articles [5]. The valence band structure of a 2D-BN triangular domain was measured by nanoARPES and is shown in Fig. 5c. It shows the expected 2D-BN band structure, with a maximum of the π and σ bands

respectively at the K and Γ points of the valence band [49-51]. Conductive AFM measurements are presented in Figs. 5e-f for a bias voltage of 1 V. The consistency between the SEM InLens image (Fig. 5d) and the c-AFM one (Fig. 5e) is obvious. The current strongly decreases when the 2D-BN thickness increases, confirming the insulating nature of the synthetised 2D-BN. An average horizontal current profile recorded in the area depicted with the dashed rectangles in Figs. 5d-e is shown in Fig. 5f. The darker area shown in Fig. 5d corresponds to the thinner BN film, with an estimated 1 ML thickness as discussed in the next section, for which the current perpendicular to the film is ~0.5 µA. This current decreases to ~70 nA for 2 ML, ~2 nA for 3 ML and is no longer measurable (below 10 pA) for 4 ML and thicker 2D-BN. Current-voltage curves were measured at some selected points in the area shown in Fig. 5e (see supplementary material part 3). From the slope of these curves in the linear part around zero bias, one may evaluate the corresponding resistances. One finds 2.0±0.7 GΩ for 2 ML 2D-BN and 10±3 GΩ for 3 ML. This resistance is larger than 1000 GΩ for 5 ML thickness and above. These figures are at least as high as the ones also measured by c-AFM on exfoliated hBN [52], emphasizing the good insulating character of the 2D-BN grown for this study. These combined Raman, cathodoluminescence, c-AFM and nanoARPES experiments clearly show the high material quality of the 2D-BN triangular domains.

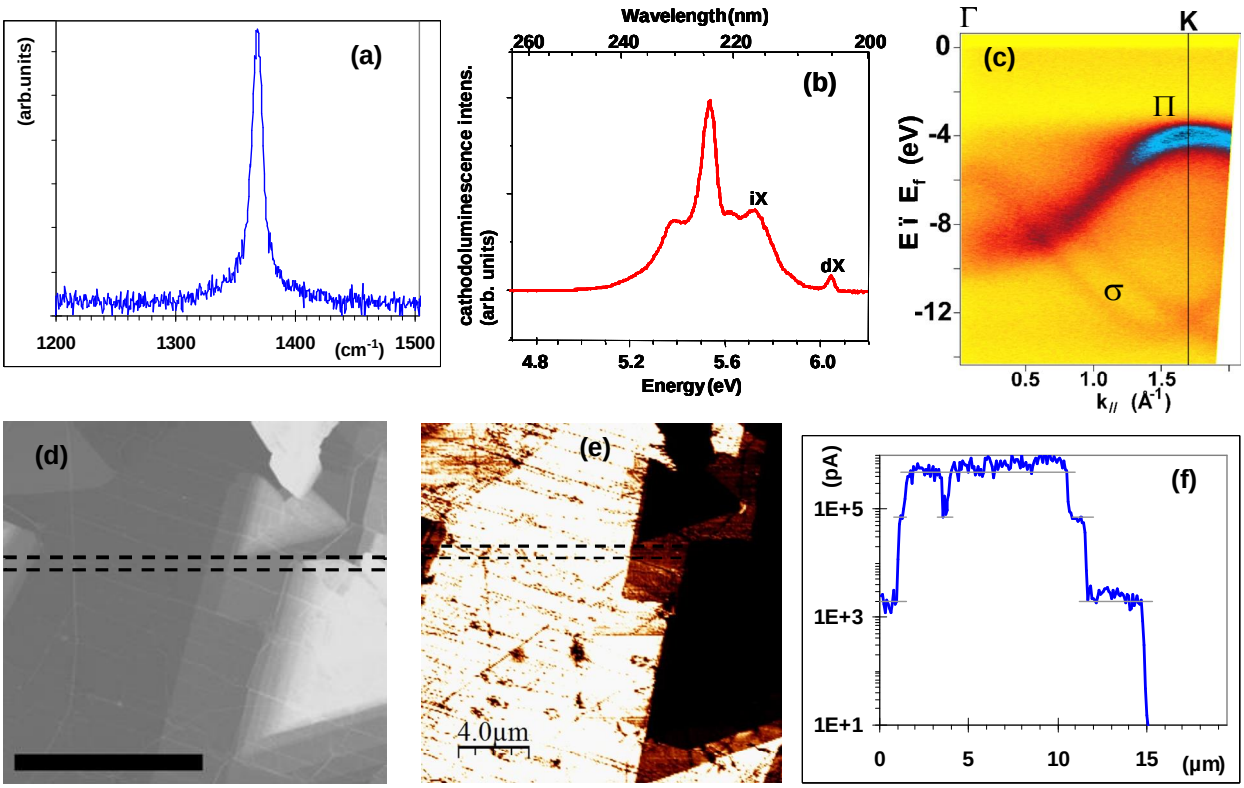

Figure 5: optimized 2D-BN growth at 910°C, measurements focused on triangular multilayer domains, typical Raman spectrum (FWHM 10-11 cm^{-1}) (a), 5 K cathodoluminescence corrected spectrum at 2 keV (b), nanoARPES valence band structure (photon energy 100 eV) (c), SEM InLens image (d) and corresponding c-AFM image (polarisation 1 V, preamplifier gain 10^9 V/A) (e). The average current is plotted in panel (f), as measured in the area bounded by the dotted lines in (d-e), using a 10^7 V/A gain. Scale bar is 10 µm (d).

3.2 Spatial distribution of BN:

The Raman peak at ~1370 cm^{-1} typical of 2D-BN is always observed in the brighter areas observed by SEM in the InLens mode, which correspond to thicker films [31], but never in the darker areas, which raises questions about the 2D-BN surface coverage. At the same time, these darker areas systematically show wrinkles after growth (see e.g. Figs. 3c, 3e and 4c), yet never on the bare Ni foils. By analogy to what is observed for both graphene and hBN [6, 53], it is suggested that these wrinkles appear during the cooling process due to differences in thermal expansion coefficients between hBN and Ni. This implies that these dark areas are also covered by a very thin 2D-BN film which is thus present on the whole surface. This conclusion is consistent with the ToF-SIMS measurements shown in Fig. S5 in the supplementary material where the $^{10}BN^-$ signal is detected over the entire analysed surface.

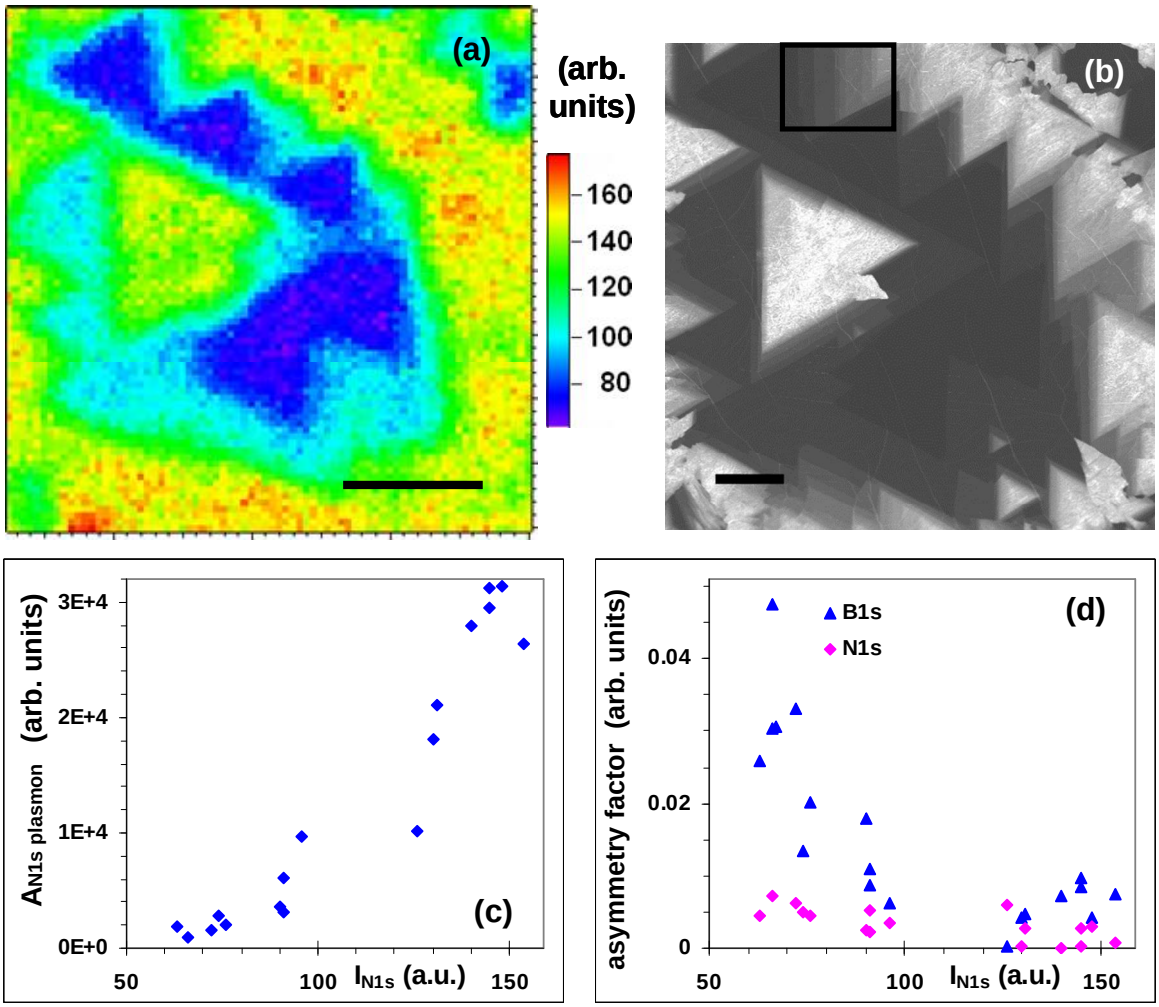

Figure 6: optimized 2D-BN growth at 910°C, N1s core level intensity map of 2D-BN on Ni foil (photon energy 700 eV) (a), SEM InLens corresponding image (b). Please notice that the minimum of the color-coded intensity in Fig. 6a is not 0 but ~60, corresponding to the minimum measured intensity. A zoom in the area delimited by the black rectangle is shown in the supplementary image S7. The π plasmon peak intensity (c) and the fitted asymmetry factor for the B1s and N1s peaks (d), as a function of the N1s intensity for high resolution spectra measured at selected points from the N1s map. Scale bars are 20 µm (a) and 10 µm (b).

Spatially-resolved photoemission measurements were realized at the Soleil synchrotron. Fig. 6a is a N1s core level intensity map in a zone where 2D-BN triangular domains of varying thickness are present. The corresponding SEM image is shown in Fig. 6b. This map confirms that nitrogen is detected everywhere on the surface, especially in the darker areas observed by SEM (another N1s intensity map recorded in a different zone is shown in the supplementary material Fig. S6). The thickness variations deduced from the N1s intensity are qualitatively consistent with the ones expected from the SEM image. From a quantitative analysis of the N1s intensity ratio in the map shown in Fig. 6a, we can conclude that the darker areas correspond to a 2D-BN monolayer thick film (see details in the supplementary material part 6). N1s and B1s local high-resolution spectra were recorded at selected points on the N1s intensity map. The difference between the energy positions of the main N1s and B1s peaks in these experiments corresponds to the expected value for BN with an average value of 207.7 ± 0.2 eV, regardless of the N1s intensity and thus of the 2D-BN thickness. Fig. 6c shows that the N1s π plasmon peak intensity increases with the N1s intensity of the main peak, therefore with the thickness of 2D-BN. For the thinnest areas corresponding to monolayer 2D-BN (where the N1s intensity in Fig. 6a is ~70), the π plasmons intensity is very close to the noise level. All N1s peaks could be rather accurately fitted by a symmetrical component in agreement with the detection of π plasmons since 2D-BN is an insulating material. However, since asymmetric components were more suitable for the B1s peaks, especially at low BN thickness, we also tried to fit the N1s peaks while imposing an asymmetric component, also using a Doniach Sunjic shape. The variations of the asymmetry factor for both peaks are presented in Fig. 6d. If the asymmetry can be neglected for thick domains (thickness ≥ 2 ML), it is systematically larger for B1s than for N1s at low BN thickness (~1 ML). This observation illustrates the complex interaction of BN at the Ni interface, suggesting a stronger bonding between B and Ni atoms than between N and Ni.

These experiments highlight that a full 2D-BN coverage is obtained, although the BN film thickness stands in a rather large range 1-15 ML. The lack of the BN Raman peak in the darker areas as shown in Fig. 6b may originate either from the low BN thickness [20] and/or from the strong bonding at the BN-Ni interface [23].

3.3 Influence of crystal orientation

Most growth experiments were performed on polycrystalline Ni foils, allowing to study the orientation-dependency of the 2D-BN structure. Fig. 7a shows an EBSD map recorded on a Ni foil after 2D-BN growth, showing zones with adjacent grains oriented along the three main Ni crystalline directions (001), (101) and (111) (see the zoom in Fig. 7b). The SEM image of the same area is shown in Fig. 7c, including labels of the Ni grain orientation as determined from the EBSD experiments. The structure of 2D-BN strongly depends on the orientation of the Ni grains. Domains show geometric shape on (001) & (101) oriented Ni grains, contrary to those observed on (111) grains where a granular distribution is observed. The E_{2g} Raman mode is detected everywhere on areas with high SEM InLens intensity, independent on the Ni orientation, but not in the darker areas which correspond to thin BN, as already mentioned in section 3.2. The corresponding Raman 2D-BN spectra show smaller widths (FWHM = 11-14 cm^{-1}) for (001) and (101) grains, while the granular grains on (111) Ni have much wider peaks (FWHM ≥ 19 cm^{-1}). This behaviour is consistent with the geometric shapes of the BN islands

and shows that the 2D-BN quality seems reduced on Ni (111) grains compared to other orientations.

Growth experiments performed on a (111) monocrystalline Ni substrate confirms this finding, showing a granular morphology of 2D-BN with grain sizes smaller than 1 µm (Fig. 8a) and wide Raman peaks (FWHM ≥ 23 cm^{-1}). Despite the small lattice parameter misfit between Ni (111) and hBN (~0.4%) [7, 8], the 2D-BN grown on Ni (111) from borazine and activated nitrogen unexpectedly shows a rather low crystalline quality. Conventional XPS measurements recorded on this sample indicate the presence of two components for N1s and B1s, well separated by a similar energy shift of ~1.7 eV (Fig. 9a-b). The respective intensity ratios of these two pairs of components B_1-N_1 and B_2-N_2 are close to 1, suggesting the presence of two configurations for 2D-BN. Considering the energy positions for BN grown on Ni foils from the only precursor borazine [23], the low binding energy B_2-N_2 pair would be associated to 2D-BN strongly bonded with Ni at the interface. In this hypothesis, the π plasmon peaks measured on the N1s and B1s spectra (Fig. 9a-b) would be associated with the high binding energy B_1-N_1 pair and not with B_2-N_2.

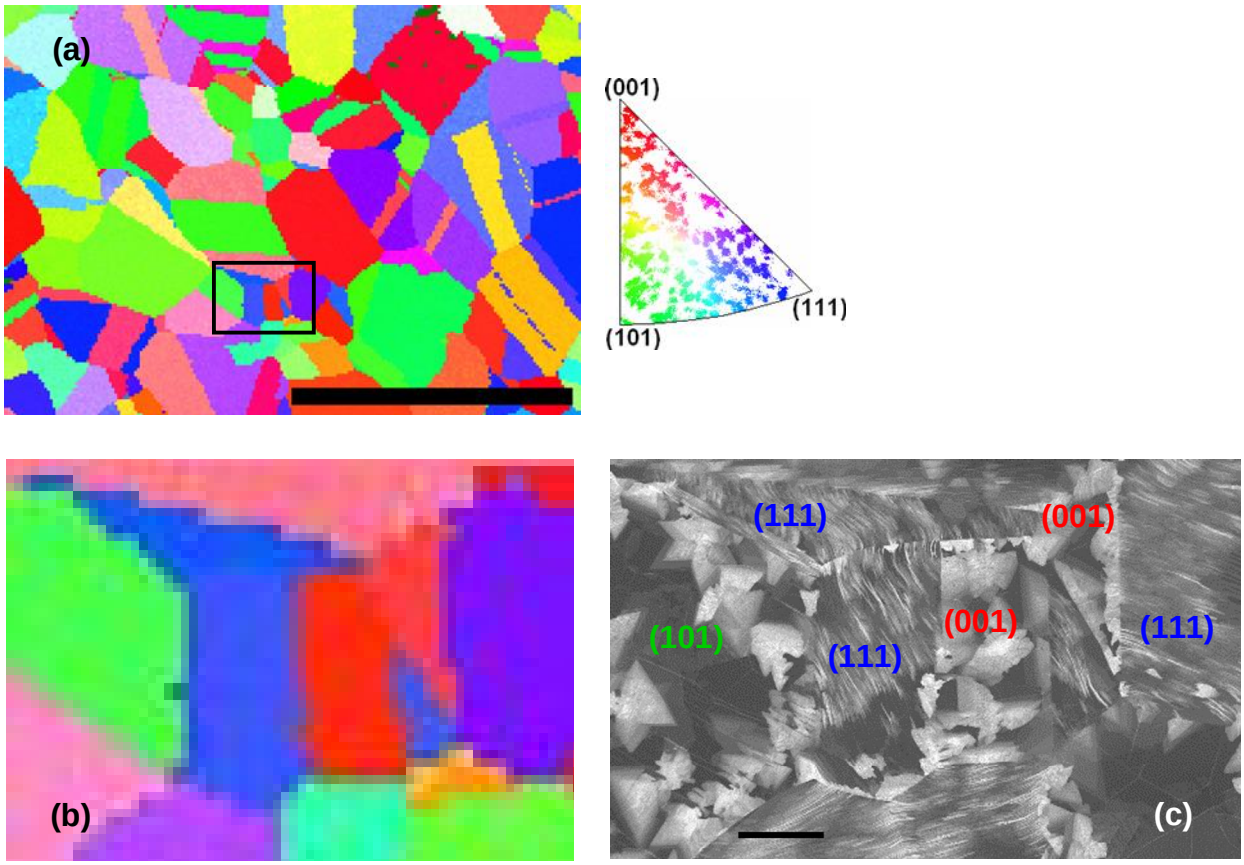

Figure 7: optimized 2D-BN growth at 910°C, EBSD mapping after growth on polycrystalline Ni and corresponding inverse pole figure (a). EBSD numerical zoom (b) in the black dashed rectangle in (a) and corresponding SEM Inlens image (c). The main crystal orientations (001), (101) and (111) are all detected in this area and labelled accordingly in (c). Scale bars are 200 µm (a) and 10 µm (c).

XPS measurements on a large (001) grain show that the B1s and N1s peaks only have one BN-related component, with a B/N composition ratio ~1 characteristic of stoichiometric BN, and that a strong π plasmon peak is detected (Fig. 9c-d). The peak positions are close to the uncoupled ones observed on Ni (111), although slightly shifted by 0.5 eV. The 2D-BN islands detected on this grain have a non-granular structure with a smaller Raman width (down to 11 cm^{-1}) than those detected on Ni (111). These observations confirm the results obtained on the polycrystalline foils, i.e. the 2D-BN crystallographic quality is lower on Ni (111) than on Ni (001) & (101). The detection of two well-separated components in XPS, one of which is associated with a strong coupling with the substrate, suggests that the growth mechanism of 2D-BN on Ni (111) probably involve some epitaxial growth mechanism. The absence of this hybridization on (001) may be at the origin of the better 2D-BN quality in this case.

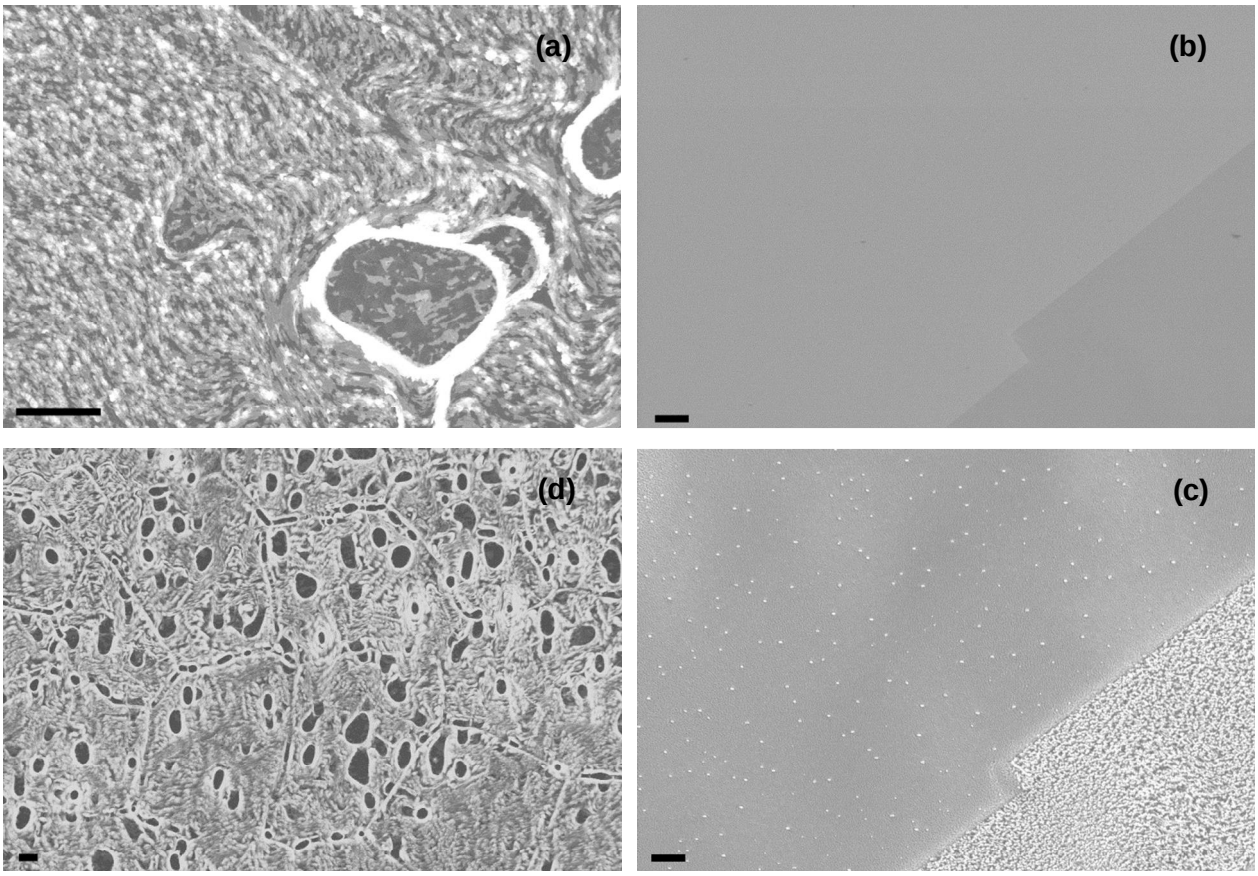

Figure 8: SEM InLens images of the granular structure after optimized 2D-BN growth at 910°C on Ni (111) single crystal (a). Reference polycrystalline Ni sample after annealing at 1000°C in the MBE chamber (b), the same sample and area after a further 1050°C anneal under H_2 (c) and the same sample after optimized 2D-BN growth at 910°C for 2 h (d). Scale bars are 10 µm (a, d) or 2 µm (b, c).

A few samples underwent a pre-anneal under H_2 at 1050°C in a separate reactor, initially intended to increase the Ni grain size [30]. Fig. 8b shows a SEM image of a sample after the standard annealing carried out at 1000°C under UHV conditions, followed by the H_2 pre-anneal (Fig. 8c). Comparison of these two images recorded at the same position of the same

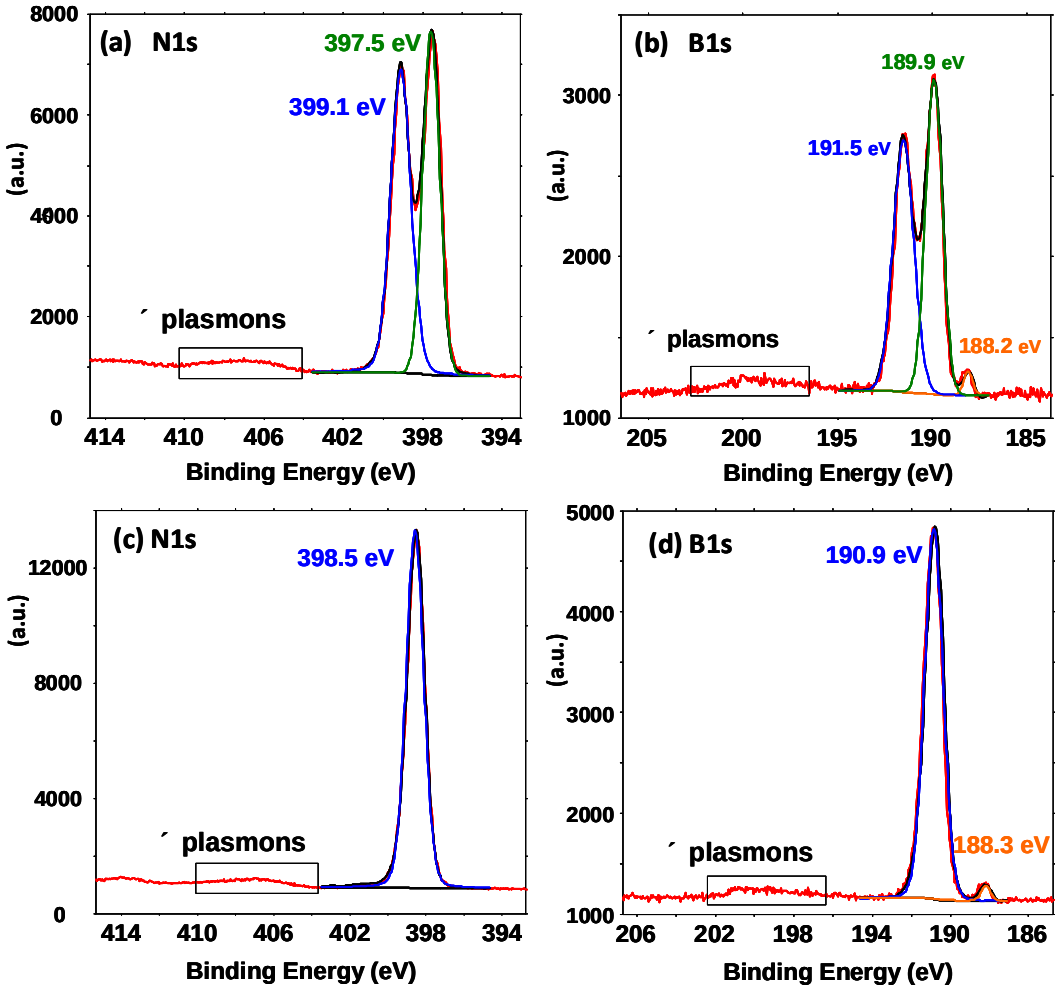

Figure 9: Conventional XPS spectra after optimized 2D-BN growth at 910°C, N1s (a) and B1s (b) on Ni (111) single crystal, N1s (c) and B1s (d) on Ni (001) single crystal. The π plasmon peaks are shown in the black rectangles. The best fits are plotted, using two symmetrical components (a, b) or one (c, d), as well as the Shirley baseline.

sample show that numerous nano-hills were generated on the foil surface during the H_2 anneal, resulting in a significant increase of the roughness. After growth of 2D-BN, the SEM observations (Fig. 8d) show that the 2D-BN granular structure previously observed only for (111) oriented domains is now present all over the foil, whatever the Ni grain orientation. The Raman peak FWHM is now rather large everywhere, ~20 cm^{-1}. XPS analysis indicates a behaviour identical to that measured on the (111) monocrystal substrate. The same pairs of components B1s and N1s are detected as on Ni (111), although with comparatively less intense Ni-bounded peaks (see the supplementary material Fig. S8). The 2D-BN thickness, as evaluated through the $d/\lambda_{B,BN}$ factor, increases from 0.60 up to 1.05 because of the H_2 pre-anneal, suggesting that the nano-hills behave as efficient nucleation sites. Under these conditions, the mean free path of ad-atoms is reduced which should result in a larger disorder at the surface. The fact that the granular structure observed on Ni (111) is identical to that after H_2 pre-anneal may suggest that the UHV annealing conditions used in this work are not sufficient to decrease the roughness of (111) oriented grains. Given the dependency of the Ni diffusion coefficient on the grain orientation [54-56], annealing at 1000°C on polycrystalline

foils would be sufficient to flatten (001) & (101) Ni grains but not the (111). A more effective surface preparation should be considered for Ni (111) surfaces, in order to obtain atomically flat terraces [8].

4. Conclusion:

By associating borazine to activated nitrogen, we have shown that it is possible to grow thicker BN films than while using borazine alone [23]. After optimization of the growth parameters, local 2D-BN triangular domains of very good quality are synthetized as shown by their geometric structure, Raman, cathodoluminescence, valence band structure and XPS spectroscopic data. The typical dimensions of these domains is limited to about 20 µm, regardless of the growth duration. The synthesized 2D-BN structure depends on the Ni grain orientation, especially the formation of bonds with Ni at the interface. This hybridization result in a complex interaction between BN and Ni. Surprisingly, despite a lower lattice mismatch, the quality of the 2D-BN grown on Ni (111) seems lower than on (001) or (101) grains, either because of the stronger coupling on (111) or of a rougher initial surface.

Acknowledgments: The financial supports by the 2DHetero FLAG-ERA project and the French RENATECH network are greatly acknowledged. The research leading to these results has received funding European Union's Horizon 2020 research and innovation program under Grant Agreement No. 881603 (Graphene Core 3). The authors thanks S. Ben Salk for providing an exfoliated hBN sample for XPS calibration.

References:

[1] C. R. Dean, A. F. Young, I. Meric, C. Lee, L. Wang, S. Sorgenfrei, K. Watanabe, T. Taniguchi, P. Kim, K. L. Shepard & J. Hone, *Boron nitride substrates for high-quality graphene electronics*, Nat. Nanotechnol. 5, 722 (2010).

[2] W. Paszkowicz, J. B. Pelka, M. Knapp, T. Szyszko & S. Podsiadlo, *Lattice parameters and anisotropic thermal expansion of hexagonal boron nitride in the 10-297.5 K temperature range*, Appl. Phys. A 75, 431 (2002).

[3] M. Pozzo, D. Alfè, P. Lacovig, P. Hofmann, S. Lizzit & A. Baraldi, *Thermal Expansion of Supported and Freestanding Graphene: Lattice Constant versus Interatomic Distance*, Phys. Rev. Lett. 106, 135501 (2011).

[4] A. K. Geim & I. V. Grigorieva, *Van der Waals heterostructures*, Nature 499, 419 (2013).

[5] L. Schué, L. Sponza, A. Plaud, H. Bensalah, K. Watanabe, T. Taniguchi, F. Ducastelle, A. Loiseau & J. Barjon, *Bright Luminescence from Indirect and Strongly Bound Excitons in h-BN*, Phys. Rev. Lett. 122, 067401 (2019).

[6] X. Li, W. Cai, J. An, S. Kim, J. Nah, D. Yang, R. Piner, A. Velamakanni, I. Jung, E. Tutuc, S. K. Banerjee, L. Colombo & R. S. Ruoff, *Large-Area Synthesis of High-Quality and Uniform Graphene Films on Copper Foils*, Science 324, 1312, (2009).

[7] A. Nagashima, N. Tejima, Y. Gamou, T. Kawai & C. Oshima, *Electronic Structure of Monolayer Hexagonal Boron Nitride Physisorbed on Metal Surfaces*, Phys. Rev. Lett. 75, 3918 (1995).

[8] W. Auwärter, T. J. Kreutz, T. Greber & J. Osterwalder, *XPD and STM investigation of hexagonal boron nitride on Ni (111)*, Surf. Sci. 429, 229 (1999).

[9] A. B. Preobrajenski, S. A. Krasnikov, A. S. Vinogradov, M. L. Ng, T. Käämbre, A. A. Cafolla & N. Mårtensson, *Adsorption-induced gap states of h-BN on metal surfaces*, Phys. Rev. B 77, 085421 (2008).

[10] S. Nakhaie, J. M. Wofford, T. Schumann, U. Jahn, M. Ramsteiner, M. Hanke, J. M. J. Lopes, & H. Riechert, *Synthesis of atomically thin hexagonal boron nitride films on nickel foils by molecular beam epitaxy*, Appl. Phys. Lett. 106, 213108 (2015).

[11] Y. J. Cho, A. Summerfield, A. Davies, T. S. Cheng, E. F. Smith, C. J. Mellor, A. N. Khlobystov, C. T. Foxon, L. Eaves, P. H. Beton & S. V. Novikov, *Hexagonal boron nitride tunnel barriers grown on graphite by high temperature molecular beam epitaxy*, Sci. Rep. 6, 34474 (2016).

[12] M. Heilmann, M. Bashouti, H. Riechert, J. M. J. Lopes, *Defect mediated Van der Waals epitaxy of hexagonal boron nitride on graphene*, 2D Mater. 5, 025004 (2018).

[13] Z. Zuo, Z. Xu, R. Zheng, A. Khanali, J. G. Zheng & J. Liu, *In-situ epitaxial growth of graphene/h-BN van der Waals heterostructures by molecular beam epitaxy*, Sci. Rep. 5, 14760 (2015).

[14] P. C. Mende, Q. Gao, A. Ismach, H. Chou, M. Widom, R. Ruoff, L. Colombo, R. M. Feenstra, *Characterization of hexagonal boron nitride layers on nickel surfaces by low-energy electron microscopy*, Surf. Sci. 659, 31 (2017).

[15] D. J. Pennachio, C. C. Ornelas-Skarin, N. S. Wilson, S. G. Rosenberg, K. M. Daniels, R. L. Myers-Ward, D. K. Gaskill, C.R. Eddy, C. J. Palmstrom, *Tailoring commensurability of hBN/graphene heterostructures using substrate morphology and epitaxial growth conditions*, J. Vac. Sci. Technol. A 37, 051503 (2019).

[16] Y. H. Lee, K. K. Liu, A. Y. Lu, C. Y. Wu, C. T. Lin, W. Zhang, C. Y. Su, C. L. Hsu, T. W. Lin, K. H. Wei, Y. Shi & L. J. Li, *Growth selectivity of hexagonal-boron nitride layers on Ni with various crystal orientations*, RSC Adv. 2, 111 (2012).

[17] H. Cho, S. Park, D. I. Won, S. O. Kang, S. S. Pyo, D. I. Kim, S. M. Kim, H. C. Kim & M. J. Kim, *Growth kinetics of white graphene (h-BN) on a planarised Ni foil surface*, Sci. Rep. 5, 11985 (2015).

[18] H. Chou, S. Majumder, A. Roy, M. Catalano, P. Zhuang, M. Quevedo-Lopez, L. Colombo & S. K. Banerjee, *Dependence of h-BN Film Thickness as Grown on Nickel Single-Crystal Substrates of Different Orientations*, ACS Appl. Mater. Interfaces 10, 44862 (2018).

[19] L. Vitos, A. V. Ruban, H. L. Skriver & J. Kollár, *The surface energy of metals*, Surface Science 411, 186 (1998).

[20] R. V. Gorbachev, I. Riaz, R. R. Nair, R. Jalil, L. Britnell, B. D. Belle, E. W. Hill, K. S. Novoselov, K. Watanabe, T. Taniguchi, A. K. Geim & P. Blake, *Hunting for Monolayer Boron Nitride: Optical and Raman Signatures*, Small 7, 465 (2011).

[21] A. B. Preobrajenski, A. S. Vinogradov & N. Mårtensson, *Ni 3d–BN π hybridization at the h-BN/Ni(111) interface observed with core-level spectroscopies*, Phys. Rev. B 70, 165404 (2004).

[22] A. Allard & L. Wirtz, *Graphene on Metallic Substrates: Suppression of the Kohn Anomalies in the Phonon Dispersion*, Nano Lett. 10, 4335 (2010).

[23] J. Hadid, I. Colambo, C. Boyaval, N. Nuns, P. Dudin, J. Avila, X. Wallart & D. Vignaud, *Molecular beam epitaxial growth of hexagonal boron nitride on Ni foils*, 2D Mater. 8, 045007 (2021).

[24] K. Watanabe & T. Taniguchi, *Hexagonal Boron Nitride as a New Ultraviolet Luminescent Material and Its Application*, Int. J. Appl. Ceram. Technol. 8, 977 (2011).

[25] L. Sponza, H. Amara, C. Attaccalite, S. Latil, T. Galvani, F. Paleari, L. Wirtz & F. Ducastelle, *Direct and indirect excitons in boron nitride polymorphs: a story of atoic configuration and electronic correlation*, Phys. Rev. B 98, 125206 (2018)

[26] H. Carrère, A. Arnoult, A. Ricard, E. Bedel-Pereira, *RF plasma investigations for plasma-assisted MBE growth of (Ga,In)(As,N) materials*, J. Crystal Growth 243, 295 (2002).

[27] K. Klosek, M. Sobanska, G. Tchutchulashvili, Z. R. Zytkiewicz, H. Teisseyre, L. Klopotowski, *Optimization of nitrogen plasma source parameters by measurements of emitted light intensity for growth of GaN by molecular beam epitaxy*, Thin Solid Films 534, 107 (2013).

[28] S. Mroz, C. Koziol & J. Kolaczkiewicz, *Carbon and sulphur on the [111] and [001] faces of nickel during thermal treatment in ultra-high vacuum and in an oxygen atmosphere*, Vacuum 26, 61 (1976).

[29] B. Dlubak, M. B. Martin, R. S. Weatherup, H. Yang, C. Deranlot, R. Blume, R. Schloegl, A. Fert, A. Anane, S. Hofmann, P. Seneor & J. Robertson, *Graphene-passivated nickel as an oxidation-resistant electrode for spintronics*, ACS Nano 6, 10930 (2012).

[30] S. Thiele, A. Reina, P. Healey, J. Kedzierski, P. Wyatt, P.L. Hsu, C. Keast, J. Schaefer & J. Kong, *Engineering polycrystalline Ni films to improve thickness uniformity of the chemical-vapor-deposition-grown graphene films*, Nanotechnology 21, 015601 (2010).

[31] P. Sutter & E. Sutter, *Thickness determination of few-layer hexagonal boron nitride films by scanning electron microscopy and Auger electron spectroscopy*, APL Mat. 2, 092502 (2014).

[32] L. Schué, *Propriétés optiques et structurales du nitrure de bore en hybridation sp^2: des cristaux massifs aux feuillets atomiques*, PhD thesis, Université de Versailles Saint-Quentin en Yvelines (2017), https://www.archives-ouvertes.fr/tel-01827237v1 .

[33] H. Chou, A. Ismach, R. Ghosh, R. S. Ruoff & A. Dolocan, *Revealing the planar chemistry of two-dimensional heterostructures at the atomic level*, Nature Comm. 6, 7482 (2015).

[34] I. Razado-Colambo, J. Avila, C. Chen, J. P. Nys, X. Wallart, M. C. Asensio and D. Vignaud, Phys. Rev. B 92, 035105 (2015).

[35] Y. Gao, Y. Zhang, P. Chen, Y. Li, M. Liu, T. Gao, D. Ma, Y. Chen, Z. Cheng, X. Qiu, W. Duan & Z. Liu, *Toward Single-Layer Uniform Hexagonal Boron Nitride–Graphene Patchworks with Zigzag Linking Edges*, Nano Lett. 13, 3439 (2013).

[36] Y. Song, C. Zhang, B. Li, G. Ding, D. Jiang, H. Wang & X. Xie, *Van der Waals epitaxy and characterization of hexagonal boron nitride nanosheets on graphene*, Nanoscale Res. Lett. 9, 367 (2014).

[37] Y. Uchida, S. Nakandakari, K. Kawahara, S. Yamasaki, M. Mitsuhara & H. Ago, *Controlled Growth of Large-Area Uniform Multilayer Hexagonal Boron Nitride as an Effective 2D Substrate*, ACS Nano 12, 6236 (2018).

[38] R. Trehan, Y. Lifshitz & J. W. Rabalais, *Auger and x-ray electron spectroscopy studies of hBN, cBN, and N_2^+ ion irradiation of boron and boron nitride*, J. Vac. Sci. Technol. A 8, 4026 (1990).

[39] D. H. Berns & M. A. Cappelli, *Cubic boron nitride synthesis in low-density supersonic plasma flows*, Appl. Phys. Lett. 68, 2711 (1996).

[40] H. Li, H. Li, W. L. Dai, W. Wang, Z. Fang & J. F. Deng, *XPS studies on surface electronic characteristics of Ni–B and Ni–P amorphous alloy and its correlation to their catalytic properties*, Appl. Surf. Sci. 152, 25 (1999).

[41] F. Muench, M. Oezaslan, M. Rauber, S. Kaserer, A. Fuchs, E. Mankel, J. Brötz, P. Strasser, C. Roth & W. Ensinger, *Electroless synthesis of nanostructured nickel and nickel-boron tubes and their performance as unsupported ethanol electrooxidation catalysts*, J. Power Sources 222, 243 (2013).

[42] P. R. Kidambi, R. Blume, J. Kling, J. B. Wagner, C. Baehtz, R. S. Weatherup, R. Schloeg, B. C. Bayer & S. Hofmann, *In Situ Observations during Chemical Vapor Deposition of Hexagonal Boron Nitride on Polycrystalline Copper*, Chem. Mater. 26, 6380 (2014).

[43] B. Feng, J. Zhang, Q. Zhong, W. Li, S. Li, H. Li, P. Cheng, S. Meng, L. Chen & K. Wu, *Experimental realization of two-dimensional boron sheets*, Nature Chem. 8, 563 (2016).

[44] C. J. Powell, A. Jablonski, *NIST Electron Effective-Attenuation-Length Database*, Version 1.3, Standard Reference Data Program Database 82, National Institute of Standards and Technology, Gaithersburg, USA, (2011). https://www.nist.gov/srd/nist-standard-reference-database-82.

[45] K. Watanabe, T. Taniguchi & H. Kanda, *Direct-bandgap properties and evidence for ultraviolet lasing of hexagonal boron nitride single crystal*, Nat. Mater. 3, 404 (2004).

[46] G. Cassabois, P. Valvin & B. Gil, *Hexagonal boron nitride is an indirect bandgap semiconductor*, Nat. Photonics 10, 262 (2016).

[47] H. Prevost, A. Andrieux-Ledier, N. Dorval, F. Fossard, J. S. Mérot, L. Schué, A. Plaud, E. Héripré, J. Barjon & A. Loiseau., *Heteroepitaxial growth of sp^2-hybridized boron nitride multilayer on nickel substrates by CVD: the key role of the substrate orientation*, 2D Mater. 7, 045018 (2020).

[48] L. Schué, B. Berini, A. C. Betz, B. Plaçais, F. Ducastelle, J. Barjon & A. Loiseau, *Dimensionality effects on the luminescence properties of hBN*, Nanoscale 8, 6986 (2016).

[49] T. Greber, L. Brandenberger, M. Corso, A. Tamai & J. Osterwalder, *Single layer hexagonal boron nitride films on Ni(110)*, e-J. Surf. Sci. Nannaotech. 4, 410 (2006).

[50] C. Chen, J. Avila, S. Wang, Y. Wang, M. Mucha-Kruczynski, C. Sen, R. Yang, B. Nosarzewski, T.P. Devereaux, G. Zhang & M. C. Asensio, *Emergence of interfacial polarons from electron-phonon coupling in graphene/h-BN van ders Waals heterostructures*, Nano Lett. 18, 1082 (2018).

[51] J. Zribi, L. Khalil, J. Avila, J. Chaste, H. Henck, F. Oehler, B. Gil, S. Liu, J.H. Edgar, C. Giorgetti, Y.J. Dappe, E. Lhuillier, G. Cassabois, A. Ouerghi, D. Pierucci, *Structural and electronic transitions in few layers of isotopically pure hexagonal boron nitride*, Phys. Rev. B 102, 115141 (2020).

[52] L. Britnell, R.V. Gorbatchev, R. Jalil, B.D. Belle, F. Schedin, M.I. Katsnelson, L. Eaves, S.V. Morozov, A.S. Mayorov, N.M.R. Peres, A.H. Castro Neto, J. Leist, A.K. Geim, L.A. Ponomarenko, K.S. Novoselov, *Electron tunneling through ultrathin boron nitride crystalline barriers*, Nano Lett. 12, 1707 (2012).

[53] K. K. Kim, A. Hsu, X. Jia, S. M. Kim, Y. Shi, M. Hofmann, D. Nezich, J. F. Rodriguez-Nieva, M. Dresselhaus, T. Palacios & J. Kong, *Synthesis of Monolayer Hexagonal Boron Nitride on Cu Foil Using Chemical Vapor Deposition*, Nano Lett. 12, 161 (2012).

[54] J. M. Blakely & H. Mykura, *Surface self diffusion measurements on nickel by the mass transfer method*, Acta Metall. 9, 23 (1961).

[55] P. S. Maiya & J. M. Blakely, *Surface Self-Diffusion and Surface Energy of Nickel*, J. Appl. Phys. 38, 698 (1967).

[56] N. Azzerri & R.L. Colombo, *Surface diffusion measurements in nickel using a modified relaxation technique*, Metallography 9, 233 (1976).

Supplementary material: Molecular beam epitaxial growth of multilayer 2D-boron nitride on Ni substrates from borazine and plasma activated nitrogen

Jawad Hadid[1], Ivy Colambo[2], Jose Avila[3], Alexandre Plaud[4,5], Christophe Boyaval[1], Dominique Deresmes[1], Nicolas Nuns[6], Pavel Dudin[3], Annick Loiseau[5], Julien Barjon[4], Xavier Wallart[1], Dominique Vignaud[1*]

[1]*Univ. Lille, CNRS, Centrale Lille, JUNIA ISEN, Univ. Polytechnique Hauts de France, UMR 8520-IEMN F-59000 Lille France*

[2]*Inst. Math. Sci. Phys., Univ. of the Philippines Los Banos, Laguna 4031 Philippines*

[3]*Synchrotron SOLEIL & Université Paris-Saclay, F-91192 Gif sur Yvette France*

[4]*Université Paris-Saclay,UVSQ, CNRS, Groupe d'Etude de la Matière Condensée, 45 avenue des Etats-Unis,78035 Versailles Cedex, France*

[5]*Laboratoire d'Etude des Microstructures (LEM), CNRS–ONERA, Université Paris Saclay, 29 Avenue de la Division Leclerc, 92320 Chatillon, France*

[6]*Univ. Lille, CNRS, Centrale Lille, ENSCL, Univ. d'Artois, IMEC-Institut Michel-Eugène Chevreul 59000 Lille France*

**corresponding author: dominique.vignaud@univ-lille.fr*

Content

1. Complementary Raman results

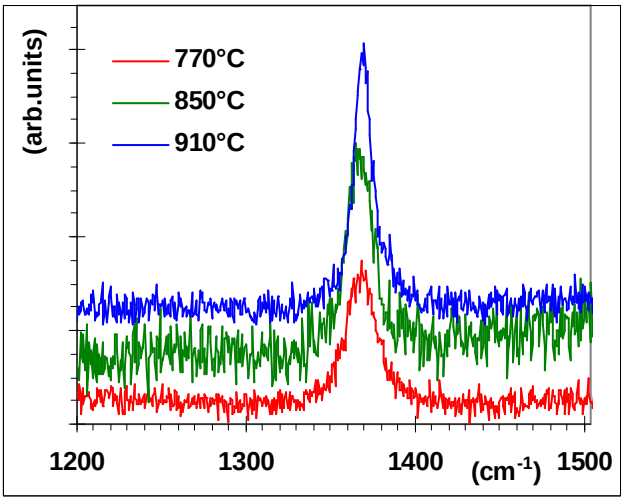

Figure S1: optimization of the 2D-BN growth versus growth temperature, typical Raman spectra. The spectra were vertically shifted for clarity.

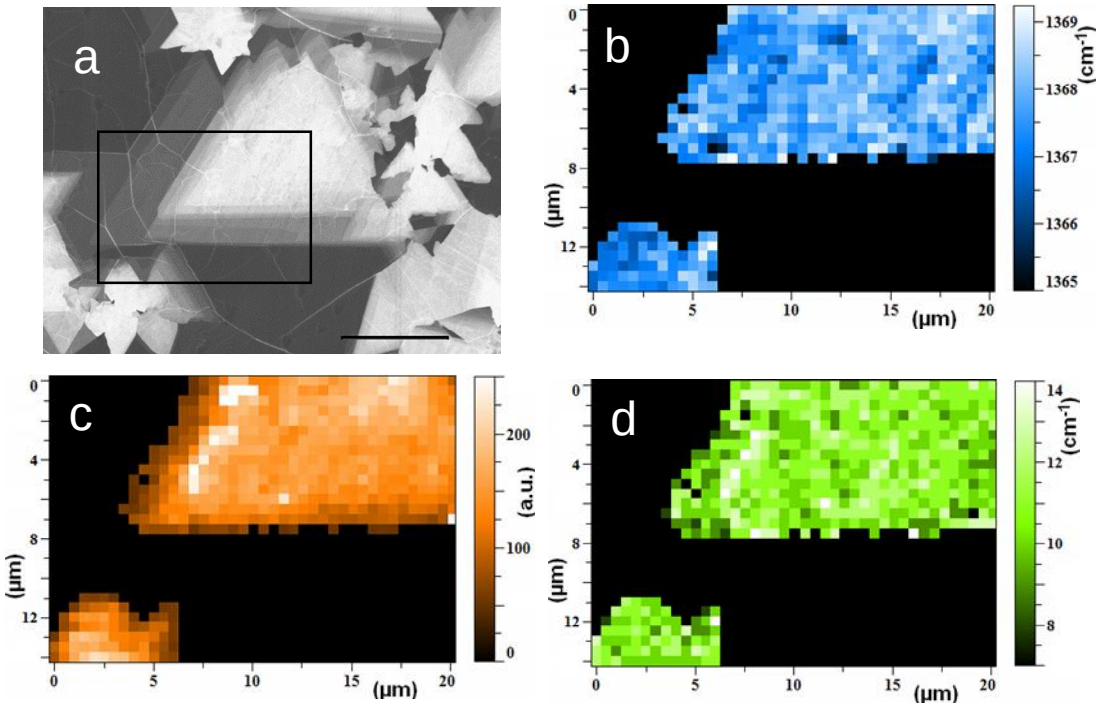

Figure S2: Raman map cartography of a triangular domain shown in the SEM image (same area already shown in Fig. 4c) (a). The black rectangle shows the area were the Raman map was measured with a 0.5 µm step. Spectral analysis using a lorentzian shape after substraction of the substrate signal, peak position (b), peak area (c) and full width at half maximum (d). No BN-related Raman component could be detected in the points which appear in black in these maps. The scale bar in panel (a) is 10 µm.

2. UV-visible large spectral range cathodoluminescence spectrum

The figure S3a shows a typical cathodoluminescence raw spectrum over the UV-visible-NIR range. The peaks appearing at ~450 and ~775 nm respectively and identified by black arrows in panel a are not deep defect-related, but comes from the 2nd and 3rd order of the main exciton-related luminescence at ~225 nm. The raw CL spectrum plotted here depends on the spectral sensitivity of the set-up. A spectrum corrected in the UV range (200-400 nm) is shown in panel b. The peak at ~320 nm (see gray arrow in Fig. S3a) disappears after correction. No defect-related cathodoluminescence could be observed in the energy band gap of such samples.

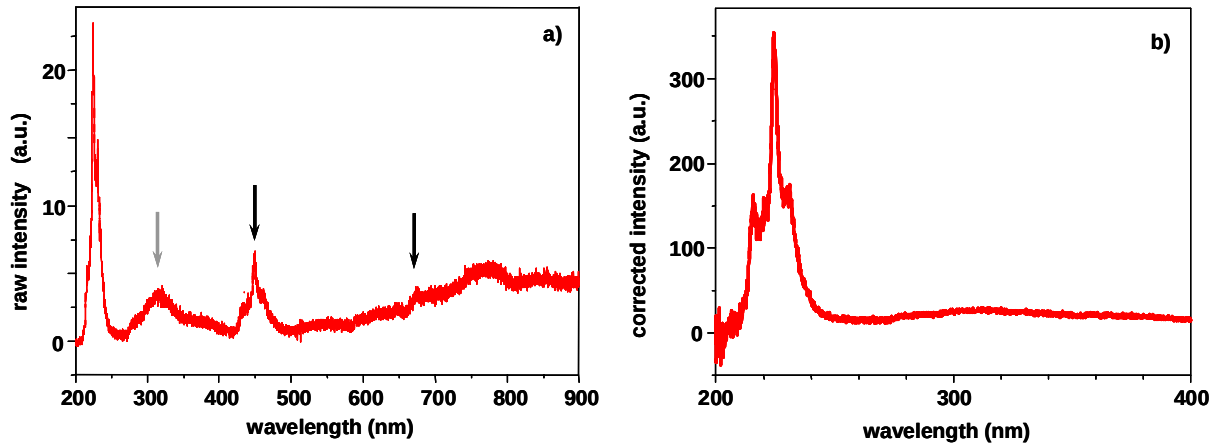

Figure S3: optimized 2D-BN growth at 910°C, cathodoluminescence raw spectrum (a) and after correction in the UV range (b), measured at 5 K (beam energy 5 keV).

3. Conducting AFM current-voltage curves

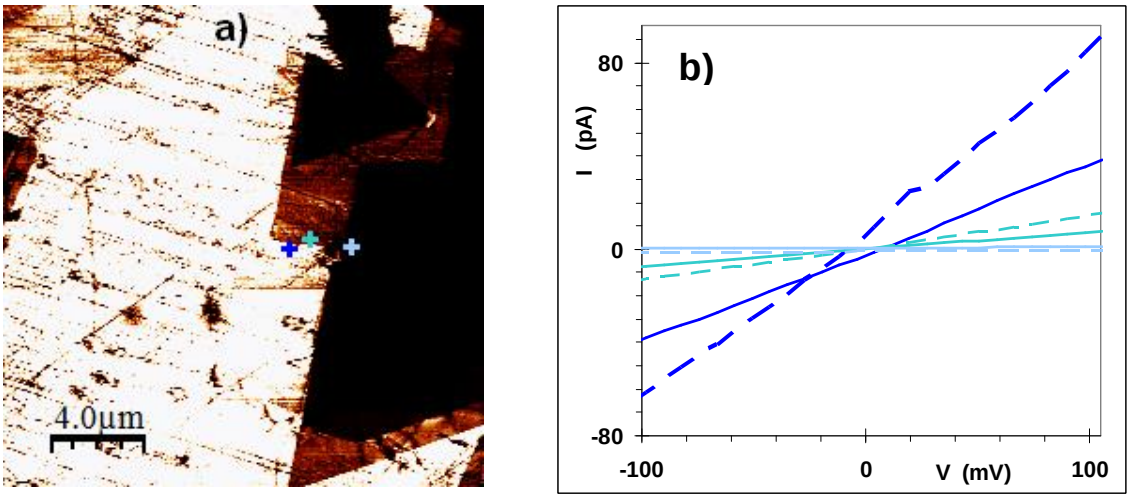

Figure S4: optimized 2D-BN growth at 910°C, measurements focused on triangular multilayer domains, c-AFM image (polarisation 1 V, preamplifier gain 10^9 V/A) already shown as Fig. 5e in the main text (a). The crosses show the location were the current-voltage curves shown in panel (b) were measured, using a 10^{10} V/A gain, for 2ML (blue), 3 ML (turquoise) and 5-7 ML (light blue). Continuous (dashed) lines were respectively measured while increasing (decreasing) the bias. The resistance quoted in the text is the average of the forward and backward slope.

4. Optimized 2D-BN growth, ToF-SIMS experiments

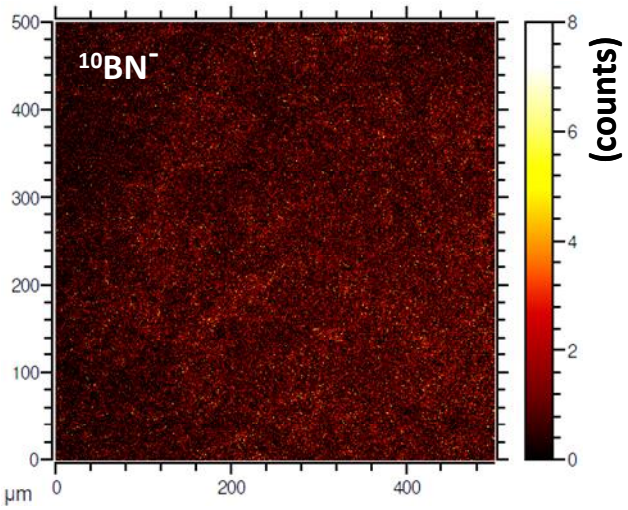

Figure S5: optimized 2D-BN growth at 910°C, ToF-SIMS map showing the total $^{10}BN^-$ signal. A full BN coverage is observed.

5. Complementary N1s intensity map

Another core-level N1s intensity map (Fig. S6d) was recorded in a different area close to the one presented in Fig. 6a. This area includes the 3 main Ni grain orientations, as shown in Fig S6c. The experimental points plotted in Figs. 6c-d includes points selected from both N1s maps.

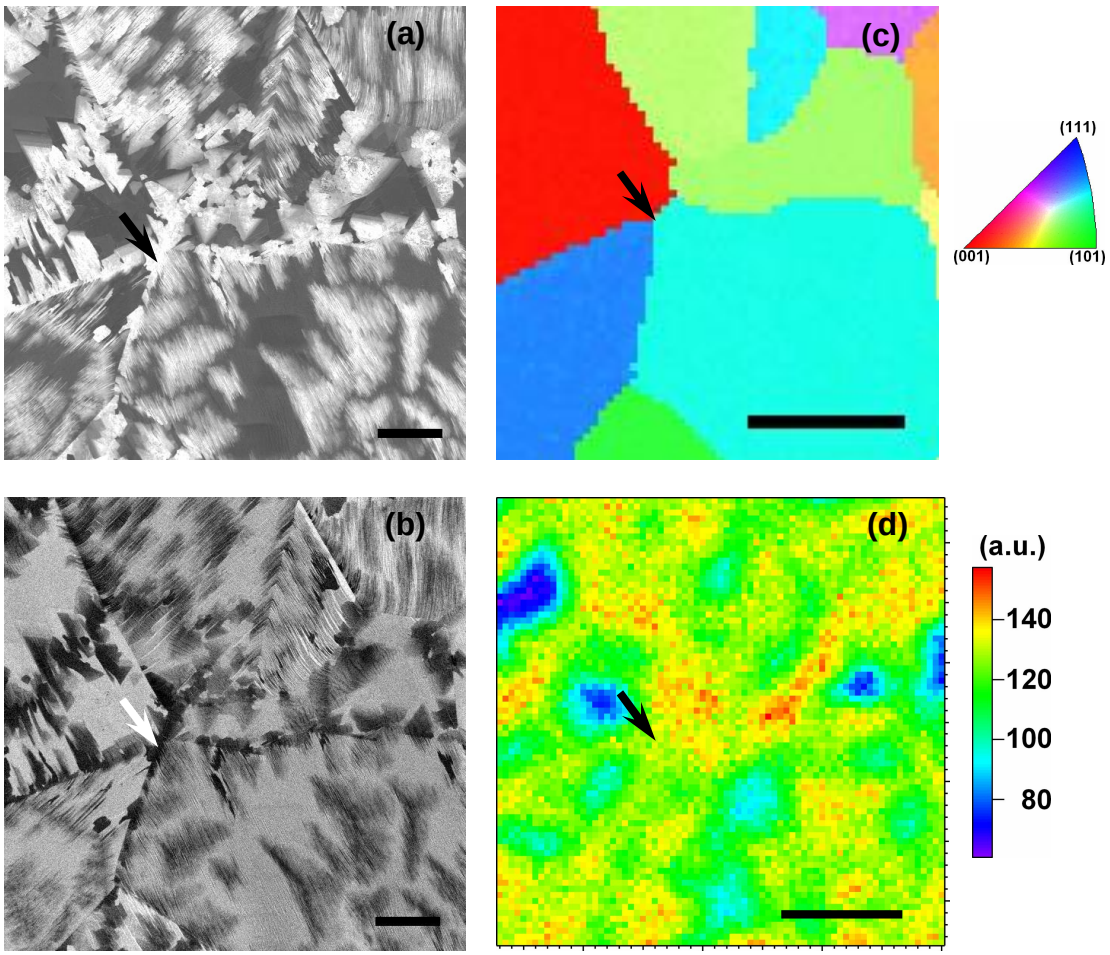

Figure S6: optimized 2D-BN growth at 910°C, same area observed in SEM InLens (a), Everhart-Thornley (b) and EBSD (c) modes, and N1s core level intensity map at a photon energy of 700 eV (d). The arrows point to the same location on the sample. The scale bars are 10 µm (a-b) or 20 µm (c-d).

6. BN thickness estimation

We detail here how the 2D-BN thickness is estimated from the N1s core level intensity mapping (Fig. 6a). The photoelectron attenuation equation is given by the following equation [1]:

$$I_{ne} = I_{\infty}\left[1 - e^{\left(-\frac{ne}{\lambda_{N,BN}\sin\theta}\right)}\right] \qquad \textbf{(S1)}$$

where $I_{n.e}$ represents the photoemission intensity measured for a n layer thick film, I_{∞} the intensity of an infinite number of layers, $\lambda_{N,BN}$ the inelastic mean free path of an electron emitted by nitrogen in BN, Θ the angle of emission (here 90°) and e the inter-planar distance in hBN (3.33 Å [2]).

ML_{max} \ ML_{min}	1 ML	2 ML	3 ML
2 ML	1.68	-	-
3 ML	2.15	1.28	-
4 ML	2.46	1.47	1.15
5 ML	2.68	1.59	1.25
∫	∫	∫	∫
15 ML	3.13	1.86	1.46
16 ML	3.14	1.87	1.46
17 ML	3.14	1.87	1.46

Table S1: Calculated intensity ratio $I_{N1s\ max} / I_{N1s\ min}$ as a function of the thickness (1–3 ML for the zone of weakest intensity and 2–17 ML for the zone of high intensity), using $\lambda_{N,BN}$=8.7 Å.

In Fig. 6a, the blue-violet zone corresponds to a zone where the N1s photoemission intensity is the lowest ($63 \leq I_{N1s} \leq 75$), so we can write $I_{N1s\ min}$ =69 ± 6 in the area where the BN layer is the thinnest. The corresponding SEM InLens image in Fig. 6b is consistent with this conclusion. The maximum N1s photoemission intensity $I_{N1s\ max}$ is 176 in the same N1s mapping (red areas), so that the experimental ratio $I_{N1s\ max} / I_{N1s\ min}$ = 2.55.

According to Ref. [3], the value of $\lambda_{N,BN}$ calculated for the 700 eV photon energy used for the N1s map is equal to 8.7 Å. Hence, we can evaluate the theoretical ratio $I_{N1s\ max} / I_{N1s\ min}$ as a function of the minimum 2D-BN thickness using the photoelectron attenuation equation (S1). These calculations are presented in Table S1, for the minimum 2D-BN thickness of 1, 2 or 3 monolayers. If we assume that the minimum BN thickness is at least 2 ML, the calculated $I_{N1s\ max} / I_{N1s\ min}$ ratio saturates at 1.87, which is inconsistent with the experimental value of 2.55. This experimental ratio is consistent with the photoelectron attenuation equation only if we assume a 1 ML thickness for the low intensity zone. However, the experimental ratio $I_{N1s\ max} / I_{N1s\ min}$ = 2.55 implies that the maximum thickness in the sample measured in Fig. 6a is 5 ML (see red square in Table S1). This contradicts the maximum layer thickness evaluated in the SEM InLens image (Figure 6b) from the step contrast which cannot be lower than 9 ML (see Fig. S6). This suggests that the blue-violet area corresponds to 1 layer of BN and that the mean free path $\lambda_{N,BN}$ must be slightly lower than 8.7 Å to probe comparatively a reduced depth. In order to solve this issue, we have calculated the $I_{N1s\ max} / I_{N1s\ min}$ ratio from equation (S1) using the experimental values of $I_{N1s\ min}$ and $I_{N1s\ max}$., assuming that the thickest area corresponds to n=9 ML. The only unknown parameter is now the inelastic mean free path $\lambda_{N,BN}$. The problem can easily be turned into a polynomial equation of degree n where the variable parameter is $X = exp(-e/\lambda_{N,BN})$, which can be numerically solved.

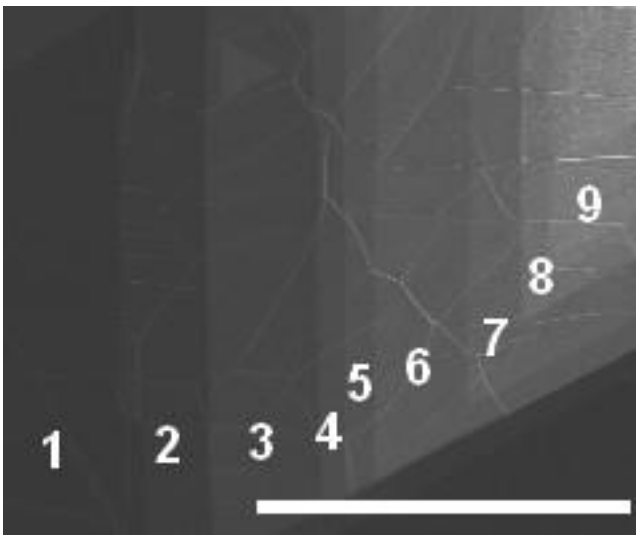

Figure S7: SEM InLens image, numerical zoom-in of the rectangular area in Fig. 6b, which shows that the 2D-BN thickness is at least 9 ML. The labels indicate the minimum thickness for each region. The scale bar is 10 µm.

In this case, the unique solution to this equation is $\lambda_{N,BN}$ = 6.8 Å if the thinnest blue-violet area corresponds to 1 ML. If one assumes that the thinnest area is 2 ML, then the solution is $\lambda_{N,BN}$ = 15.7 Å. This last value appears too shifted from that calculated [3] to be realistic, which implies that the thinnest 2D-BN area in Fig. 6a is 1 monolayer thick.

7. XPS spectra of 2D-BN grown on H2 pre-annealed Ni foils:

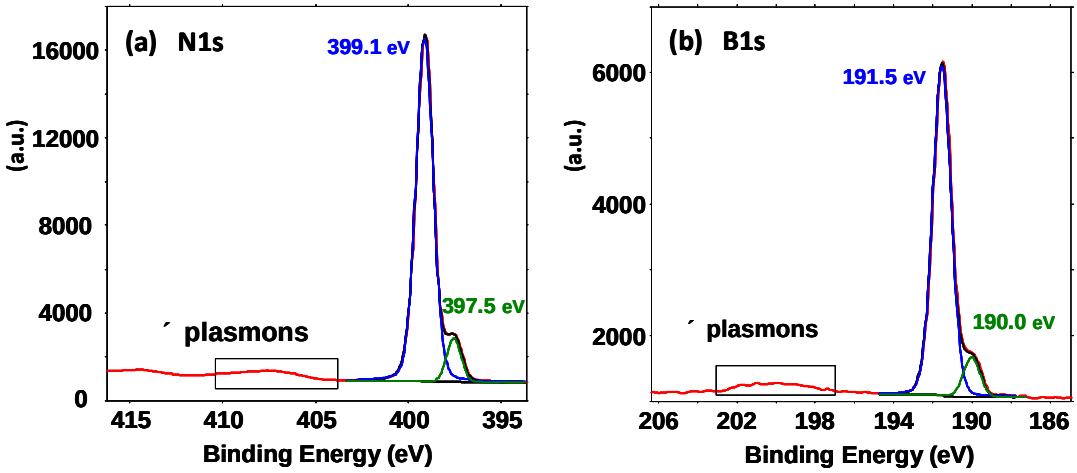

Figure S8: XPS core level spectra for N1s (a) and B1s (b) after 2D-BN growth for 2 hours at 910°C on a Ni foil pre-annealed under H_2. The π plasmon peaks are shown in the black rectangles. The best fits, using two symmetrical components for both cases, are shown, as well as the Shirley baseline.

References:

[1] M. P. Seah, *Surface Analysis by Auger and X-Ray Photoelectron Spectroscopy (The Cromwell Press, Trowbridge)*, Chap. 13, Sec. 13.5, p. 369, (2003).

[2] M.I. Petrescu & M.-G. Balint, *Structure and properties modifications in boron nitride. Part I: Direct polymorphic transformations mechanisms,* UPB Sci. Bull. B 69, 1454 (2007).

[3] H. Shinotsuka, S. Tanuma, C. J. Powell & D. R. Penn, *Calculations of electron inelastic mean free paths. XII. Data for 42 inorganic compounds over the 50 eV to 200 keV range with the full Penn algorithm*, Surf. Interface Anal., 51 427, (2019).